Cloud-Field Variability from Ground-Based Lidar and Radar Observations

D.P. Donovan and A.C.A.P. Van Lammeren, KNMI, Postbus 201, 3730 AE De Bilt, the Netherlands (donovan@knmi.nl)

H. Russchenberg, IRCTR, T.U. Delft, the Netherlands

A. Apituley, RIVM, Bilthoven, the Netherlands

Introduction

Cloud-variability has obvious implications with regards to synergetic cloud remote sensing. By combining measurements made with different instruments in principle it is possible to extract much more information than is the case by using each instrument in isolation. However the different instruments may have different footprints and sampling rates as well there may be some spatial and/or temporal separation between the measurements made by the different sensors. Hence, it is necessary to know to what extent two spatially and temporally separated soundings may be meaningfully compared. To further complicate matters, the degree of signal variability in space and time depends not only on the physical variability of the cloud field itself but also on what exactly a given instrument is measuring.

Such cloud-variability considerations play an important role with respect to the proposed Earth Radiation Mission (ERM) where flying different instruments on different co-orbiting platforms is being considered (see Fig. 1). It is important to quantify what errors may result from a given time and spatial separation between the passage of the different instruments over a given cloudy volume.

Ground-Based Measurements

Ground-based lidar and radar measurements, such as those made during the Netherlands CLoud And Radiation experiment (CLARA) [Lammeren et al. 1996] and CLARE'98 can be used as a basis for investigating cloud-variability effects. During the third CLARA campaign two nearly identical lidars were operated within 4 km of each other on a continuous basis. The ESTEC-CT75 lidar was operated at the main CLARA site in Delft while the KNMI lidar of similar type was operated about 4 km away. So, in this study we are able to explore two avenues with regard to assessing the effects of cloud-field variability, namely:

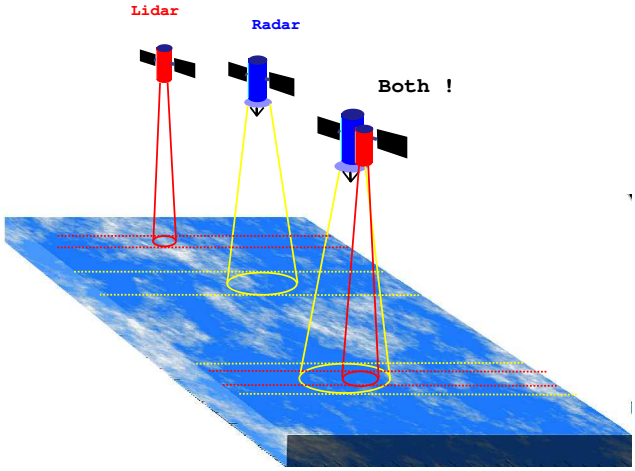

Figure 1: Split-mission vs. single platform scenarios for the ERM.

- The effect of a known spatial separation
- The effect of a (simulated) temporal separation

We will first discuss the results of the comparison

between the separated KNMI and ESTEC lidars during CLARA. Then we will discuss the general temporal behavior of the signals using both lidar and radar signals acquired during CLARA as a whole. Finally, we will use the results of the investigations into the general behavior of the observed signals as the basis for conducting simulations aimed at predicting the effect of different sampling parameters (e.g. instrument footprint, spatial separation) with respect to a space-based lidar/radar instrument.

Spatial Separation

As a illustrative example we will present CLARA data from November 20 taken with the separated lidar systems. Fig. 2 shows the time-height lidar signals for both lidars on this day at full resolution (12.5 meters and 30 seconds). At the scale of the color images not much difference can be discerned between the two images. On this day, Delft was near the center of a low pressure system [Donovan et al, 1999] and the cloud cover was somewhat sporadic with most of the clouds being between 1 and 2 km.

Fig. 3 shows two constant altitude cross-sections through Fig. 2 for 0.5 km and 1.8 km. The slice at 0.5 km is below the bulk of the clouds and the backscatter is likely mainly due to boundary layer aerosols while the 1.8 km slice goes through the bulk of the clouds. Evidently the signals at 0.5 km are well correlated, however at 1.8 km the situation is less clear. At 1.8km, the signals are both sporadic and not necessarily in good correspondence with each other.

A space-based lidar would not make measurements with such a high resolution as the data shown in Fig. 3, but instead it would perhaps have a measurement resolution of 100 meters in the vertical and about 5 km in the horizontal. So it is useful to compare the two separated lidar returns rebinned to a resolution comparable to that that may be envisioned for a space-based instrument. Degrading the vertical resolution is trivial. However, simulating a given horizontal resolution is impossible without making some assumptions first. First we must assume that the cloud field at some scale varies the same in time as it does in space and secondly we must choose some relationship between the time and space coordinates. Here we have chosen to simply use the mean wind speed to relate the time and space coordinates. Here the winds at 1 km were on the order of 25 km per hour so that a temporal resolution of about 0.2 hours should be comparable to a horizontal resolution of 5 km.

The same data as shown in Fig. 2 are shown in Fig. 4 but at low resolution. Fig. 5 shows an example low resolution signal profile for both the KNMI and ESTEC lidars at about 20 UTC. Here it is obvious that the high resolution profiles for each lidar are notably different from each other. It may be supposed that rebinning the data to degrade the resolution may remove the differences. However, it can be seen that the low resolution profiles still retain differences.

Low resolution signal cross-sections for 0.56 and 1.8 km along with the correlation coefficient between the low resolution KNMI and ESTEC signals are shown in Fig. 6 . Here ρ refers to Pearson's correlation coefficient, which in general can be written (with respect to two random variables x and y) as:

$$\rho = \frac{\sum_i (x_i - \overline{x})(y_i - \overline{y})}{\sqrt{\sum_i (x_i - \overline{x})^2 \sum_i (y_i - \overline{y})^2}} \qquad (1)$$

where the bars denote averages and the subscripts refer to the measurment index. As can be expected from Fig. 3 at 0.56 km the correspondence is good $\rho = 0.90$ while even at low resolution the correspondence at 1.8 km is fairly low with a correlation coefficient of about 0.77.

Fig. 7 shows the height dependent correlation coefficients derived in a manner similar to those presented in Fig. 6. The average signal profiles for the KNMI and ESTEC lidars along with the maximum and minimum signal envelopes are also shown in Fig. 7 . It can be seen that at certain altitudes there is a very good correspondence between the measurments made by the separated lidars while at other altitudes the correspondence is quite low. In general, most of the correlation coefficients are above 0.7 but there is a wide range of scatter. The same analysis as presented here was performed on all the days in which data from both lidars was available (about 6 days). For all the cases considered, which spanned a variety of conditions, correlation coefficients around 0.8 were most common with a wide degree of scatter being usually present. Evidently then, 4 km appears to be a "medium" spatial separation compared to the mean correlation distance for the cases considered here.

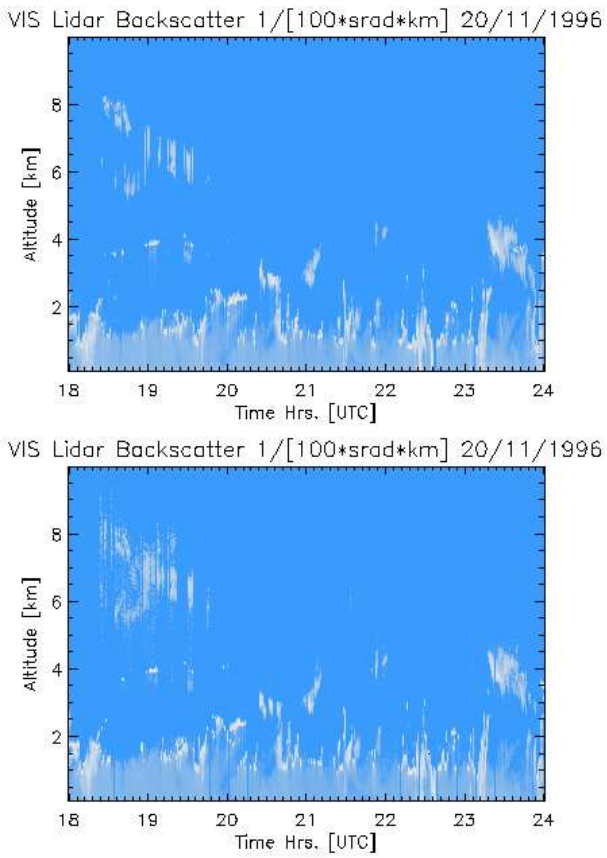

Figure 2: KNMI and ESTEC lidar signals for November 20th, 1996 (CLARA). Both lidars were of the same type (Vaisala CT–75K) but the KNMI lidar was located approximately 4 km from the main CLARA site. The upper image is for the ESTEC lidar while the lower image is for the KNMI lidar.

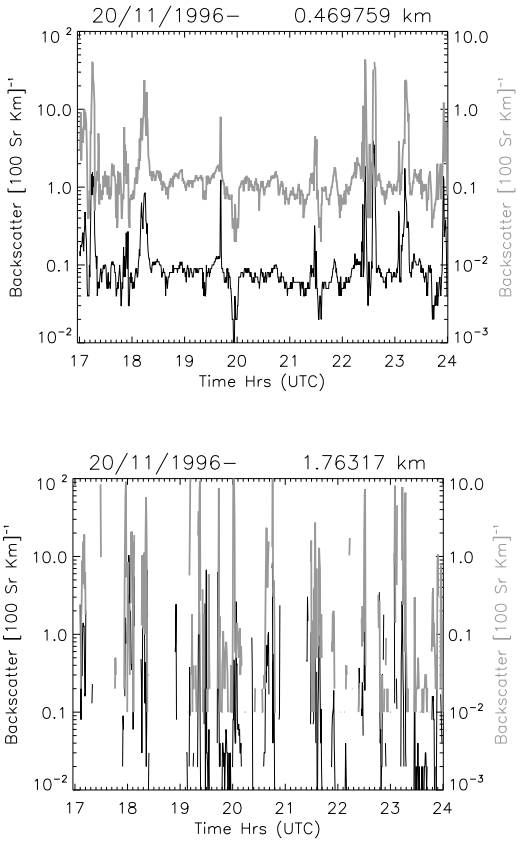

Figure 3: High resolution signal cross for the KNMI and ESTEC lidar signals for November 20, 1996 (CLARA) for 0.5 and 1.8 km respectively. The Grey line is for the KNMI lidar signals while the dark line shows the ESTEC lidar signals.

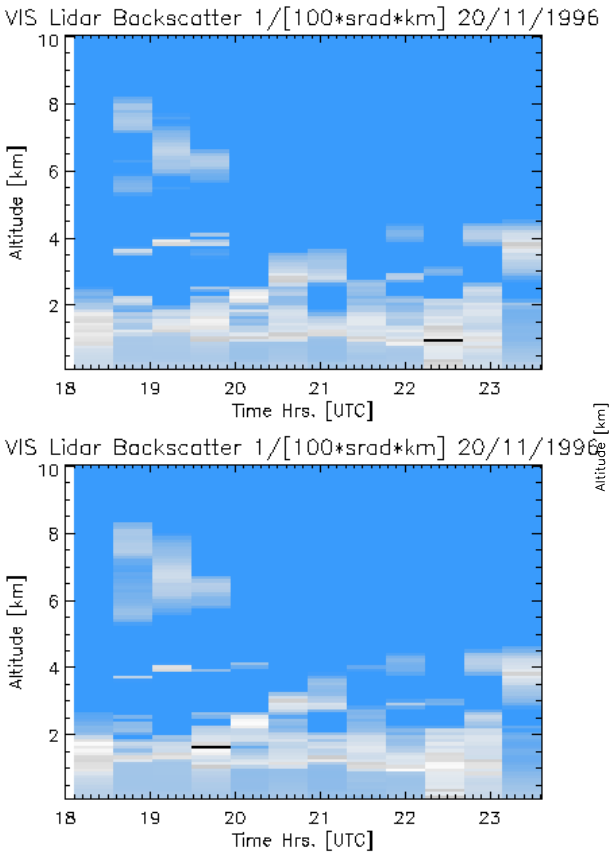

Figure 4: The same lidar signals as shown in Fig. 2 but rebinned to a much lower resolution. Here the vertical resolution is 100 meters while the temporal resolution is 12 min. The upper image is for the ESTEC lidar while the lower image is for the KNMI lidar.

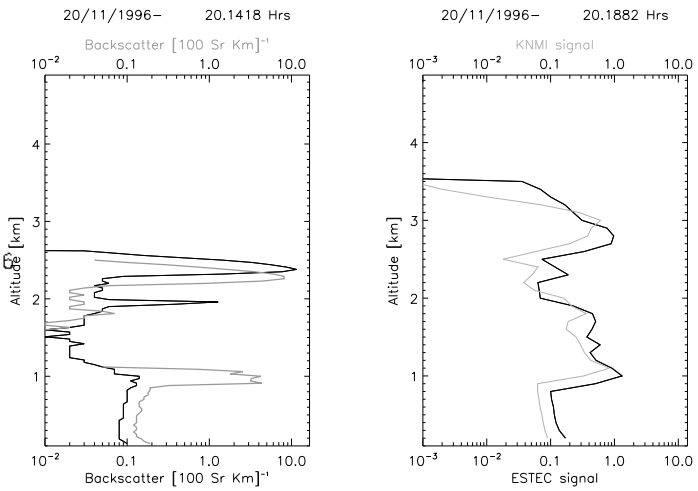

Figure 5: High resolution (Right) and low resolution (Left) signal profiles for 20.18 hours The Grey line shows the profile for the KNMI lidar while the darkline shows the signals for the ESTEC lidar.

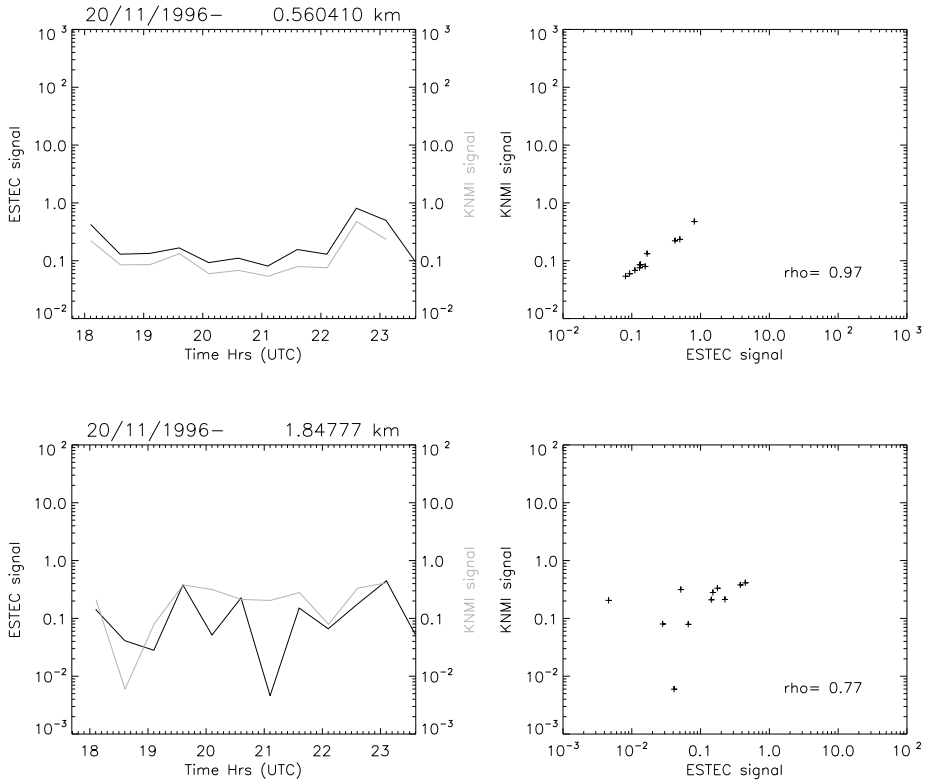

Figure 6: Low resolution time series of signals at 0.56 km (Top-Left) and (Top-Right) the signals plotted as a function of each other. The bottom panels are for 1.8 km. The Grey line corresponds to the the KNMI lidar while the darkline shows the signals for the ESTEC lidar.

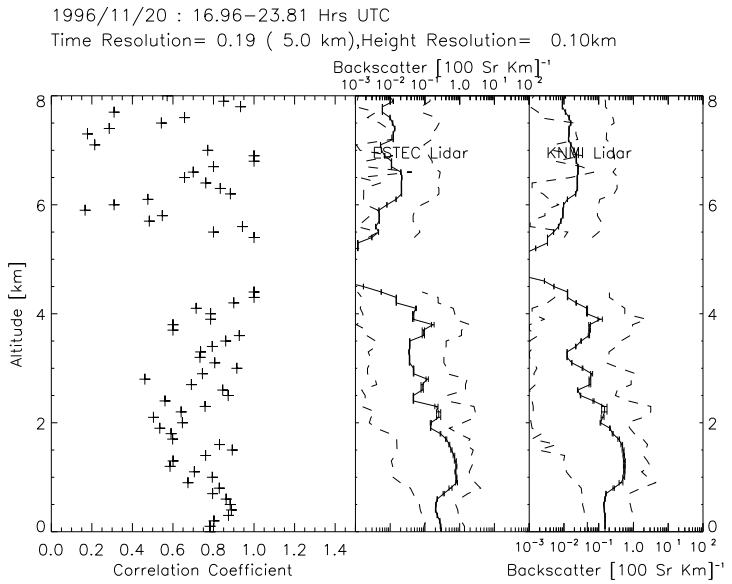

Figure 7: Average signals for the KNMI and ESTEC lidars (Middle and Left). The error bars give the standard deviation of the average while the dashed lines show the minimum and maximum signal envelops respectively. The plus marks (Left) show the altitude dependent correlation coefficients.

Single Instrument Time Series

Here we will address the question of cloud variability using information that may be obtained by using single instrument signal time series. We are interested in using the ground-based single instrument time series to aid in characterizing the errors that could arise from comparing space-based measurements that have been obtained at different times and for slight different orbit tracks. Example time series for April 18th and November 29th, 1996 (CLARA) are shown in Figs. 8 and 9. An obvious first course of action is to examine the effect of applying a time shift to the same data time series. In principle this is easy to do; one just compares the relative differences between the unshifted time series and a series of identical but shifted (in time) series. i.e.

$$< RelativeError(k) >= \frac{\left[\sum_0^N (S_i - S_{i+k})^2\right]^{1/2}}{sum_0^N S_i} \quad (2)$$

where k is the number of shifted indices such that $\delta t = k * dt$. If we assume that the effect of a spatial offset (δx) may be approximated by a time shift of $\delta t = \delta x / v$, where v is some *scene velocity* we may also investigate the effects of spatial separations in an approximate manner.

Since the expected resolutions of the instruments on the ERM are much smaller than those of the ground based instruments used here the results must be extrapolated to the resolution we expect for the space-based observations. To do this, it is not advisable to smooth the signals to space-resolution and then find the relative differences between the shifted and unshifted signals. This is due to the fact that by smoothing the time series one will average over the same data between the shifted and unshifted signals. This will not occur in the situation we are trying to simulate (that of two co-orbiting platforms). However, we can employ an alternative approach to extrapolating the high resolution observed differences to lower resolutions by simply assuming that the observed relative error will decrease with increasing sample size. i.e.

$$\begin{aligned} < RelativeError_N > &= \left[\frac{N1}{N}\right]^{1/2} \\ &\times < RelativeError_{N1} > \end{aligned}$$

Fig. 10 shows the expected average relative error as a function of time delay for different resolutions for the data shown in Fig. 8. Given a mean scene velocity of about 10 meters per second (similar to the wind speed at this altitude measured by local radiosondes) the upper curve is appropriate for a space-based resolution of about 300 meters while the lowest curve is appropriate for a resolution of about 1.2 km. In Fig. 10 it can be seen that the error increases rapidly with temporal delay, reaching a maximum after about 0.5 hours. Fig. 11 is similar to Fig. 10 except that it corresponds to the data shown in Fig. 9 here the errors are generally much more than those shown in the previous example and the maximum errors are reached after only about 6 minutes or so.

The approach outlined so far is somewhat limited as there is no real way to incorporate the effects of instrument differences and combined spatial and temporal offsets in a logical fashion. Also, it would be difficult to assess issues such as instrument footprint size using this approach. To more beyond we need to examine the intrinsic characteristics of the signals themselves. Once we have amassed enough information on the inherent scales and variances of the lidar and radar signals we can use this information as the basis for conducting full 2-dimensions simulations in a more rational manner.

In the next section we will treat the lidar and radar signals as standard time series and derive such quantities as the correlation time and the exponent of the *power spectral density*. Since cloud fields self-similar to some degree, that is, at large scales they similar to the way they do at small scales, we will also employ some statistical methods that are useful when analyzing *fractal* signals.

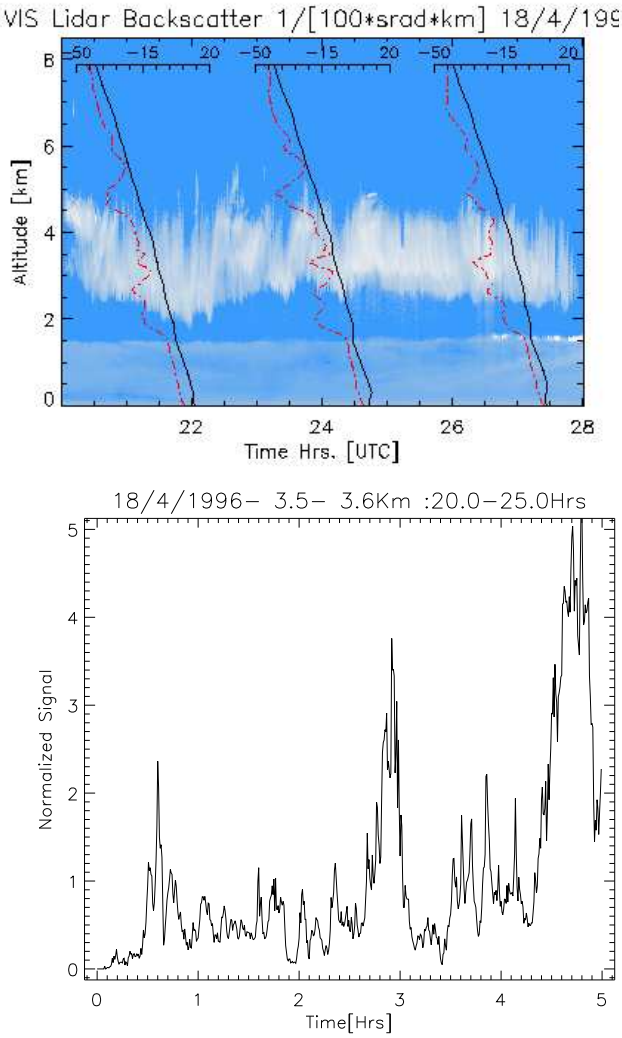

Figure 8: Lidar signals along with temperature (dark line) and dew point (red line) profiles extroplated from sonde measurements (top panel). Sample signals time series take through the main cloud (bottom).

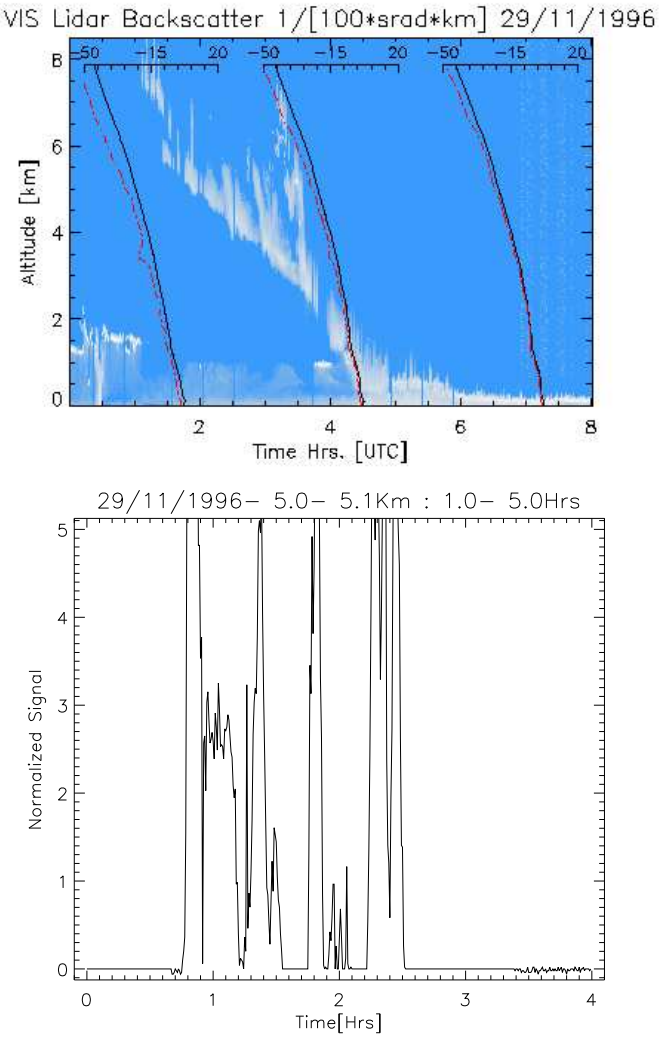

Figure 9: Lidar signals along with temperature (dark line) and dew point (red line) profiles extroplated from sonde measurements (top panel). Sample signals time series take through the main cloud (bottom).

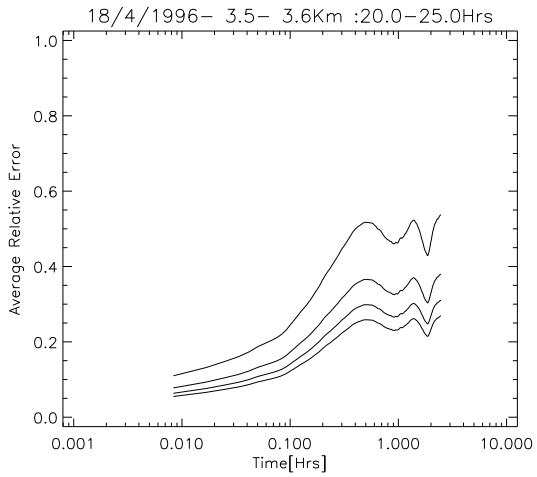

Figure 10: Relative error as a function of delay for different sampling resolutions for the time series shown in Fig. 8 (April 19th). From 300 meters (topcurve) to 1200 meters (lowest curve).

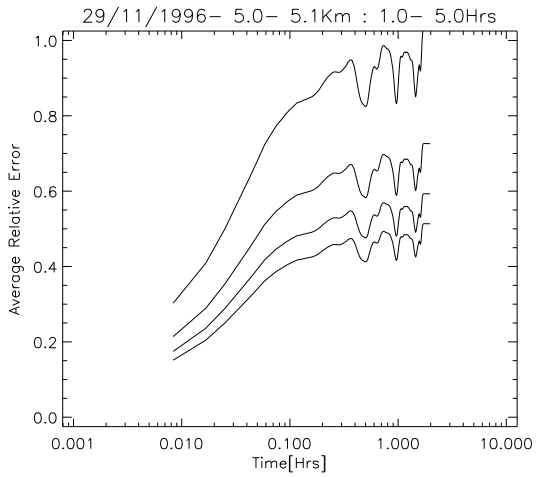

Figure 11: Relative error as a function of delay for different sampling resolutions for the time series shown in Fig. 9 (November 29th). From 300 meters (topcurve) to 1200 meters (lowest curve).

Spectral Analysis

In Fig. 12 the radar and lidar signals for April 19th are shown while in Fig. 13 an example normalized constant altitude signal cross-section is shown. The cossesponding power spectral density (PSD), the autocorrelation, and a modified form of the so-called *second order structure function* [Davis et al. 1996] are shown are also shown in Fig. 13. The power spectral density is a measure of the power present in the time series as a function of frequency and is deduced using standard Fourier analysis techniques. The autocorrelation function is defined as:

$$ACorr(T_n) = \frac{\sum_{i=0}^{N-n-1}(X_i - < X >)(X_{i+n} - < X >)}{\sum_{i=0}^{N-1}(X_i - < X >)^2} \quad (3)$$

where X_i denotes the ith point of the time series and the braces <> are used to denote averages. In Fig. 13 we also shown the square root of the structure function $D(T_n)$ here defined as

$$D(T_n) = \frac{< (X_{i+n} - X_i)^2 >}{< X^2 >} \quad (4)$$

The PSD, autocorrelation function, and the structure function are all related to each other and give complementary information. For fractal signals $D(T_n)$ often possesses a regime where it follows a power law, that is:

$$D(T_n) \propto T_n^H \quad (5)$$

It can be shown [Davis et al. 1996] that this implies that the PSD will also follow a power law with exponent $\beta = 2H + 1$. Generally H will be equal to 2 for processes resembling Brownian motion while H will equal 0 for white noise.

In Fig. 13 we see that that D indeed does obey a power law with $H = 0.5$ for T_n less than about 0.08 Hrs while for T_n greater that about 0.2 Hrs D is nearly flat ($H = 0$). By referring to the correlation coefficient it can also be seen that the point where D "becomes flat" corresponds roughly to the point where the autocorrelation becomes 0. This example clearly shows that for 2 points in this radar signal time series to be considered to be correlated (**Acorr** > 0.9) they must, in general be separated by no more than 0.01 Hrs (about 30 seconds). This small separation is still well above the sampling interval of the radar used here (5 seconds).

Fig. 14 shows the lidar signals time series analysis corresponding to Fig. 13. Here the spectral exponents are similar to those for the corresponding radar time series. The correlation length is slightly

larger though. Here D follows a power law until T_d equals 0.3 Hrs where it abruptly departs (a so-called 'scale-break'). In general, the lidar and radar respond to particles in fairly different size regimes. Roughly speaking, the lidar backscatter goes as the particle radius to the 2nd power while the radar backscatter scales as the particle radius to the 6th power. This difference in response can be expected, in general, to given rise to different exponents and correlation times for the lidar and radar signal time-series even though the lidar and radar measurements may be co-located. Although here the exponents between the lidar and radar are very similar. This may imply, that in the case shown in Fig. 14, that average size of the cloud particles was fairly constant with time.

The similarity between the radar and lidar signal statistics presented in Figs. 13 and 14 for April 18th is contrasted by the data shown in Figs. 15-17 for April 23rd. Here the radar signals are very weakly correlated with a scale-break occurring around 0.02 hours for the Radar signals. For the lidar signal time-series, the scale-break occurs near 0.2 Hrs with high values of **ACorr** being present out to 0.1 hours. In this example, there were clearly large cloud particles present and the average size of the cloud particles must have changed with time giving rise to the differences in behaviour between the lidar and radar signal time-series.

In Figs. 18–20 a final example is presented. Here the results of analyzing 2 radar time series both at the same times but for different altitudes are shown. Fig. 19 shows the results of the analysis of a time series taken above the peak return while 20 shows the results for a time-series taken at the peak return altitudes. The time series centered at 2.1 Km is dominated by the strong return at 1.8 Hrs while the time series at 0.6 km is not dominated by any single strong event. Here the scaling exponents are seen to be different and the correlation ranges are also seen to be different. The correlation coefficient curves for these two altitudes are also of different character. The upper altitude time series is highly correlated at short time scales but quickly becomes uncorrelated. The lower altitude time series is not as strongly correlated for small temporal separation but the correlation coefficient does not become 0 until nearly 1 hour.

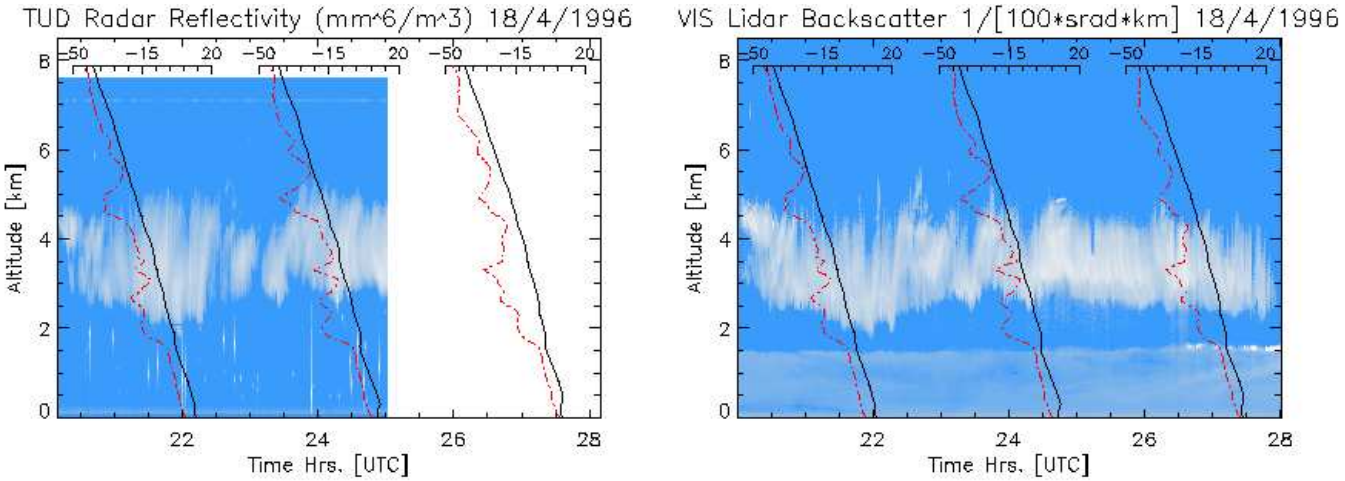

Figure 12: Radar (Left) and lidar (Right) signals for April 18, 1996 (CLARA).

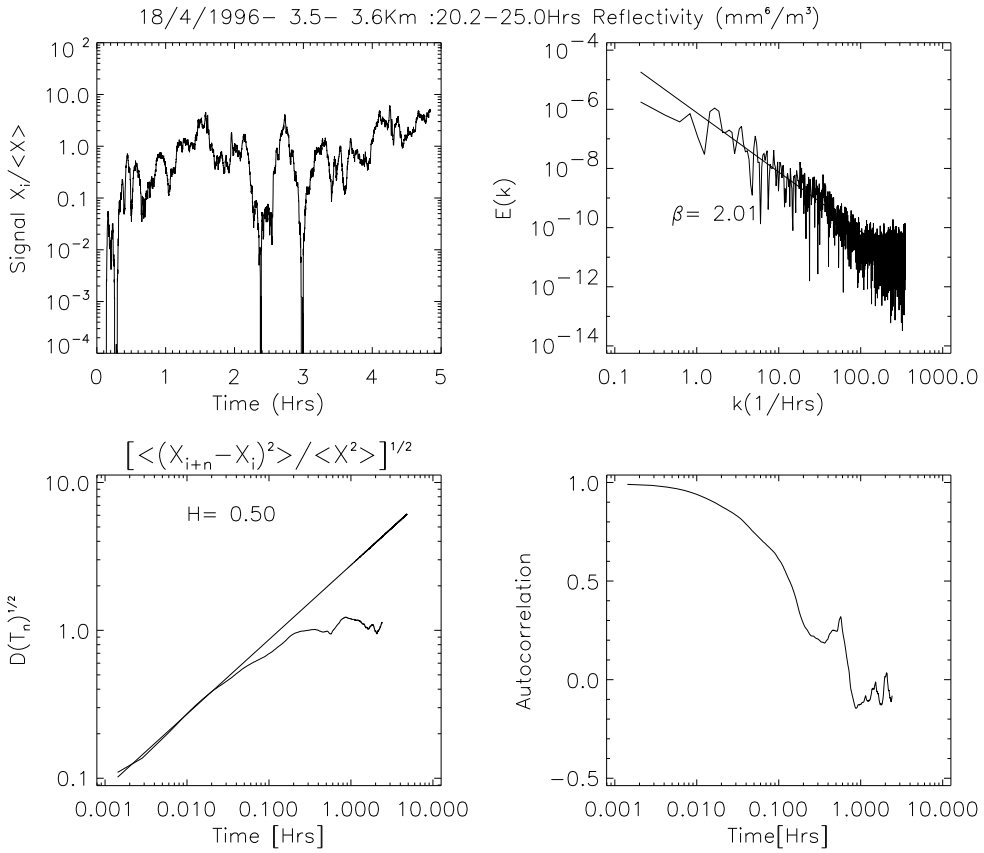

Figure 13: Spectral analysis results for radar signals for April 18th. The normalized signal ($X/ < X >$, Top left) the PSD (Top Right), the structure function (Bottom Left) and the autocorrelation (Bottom Right).

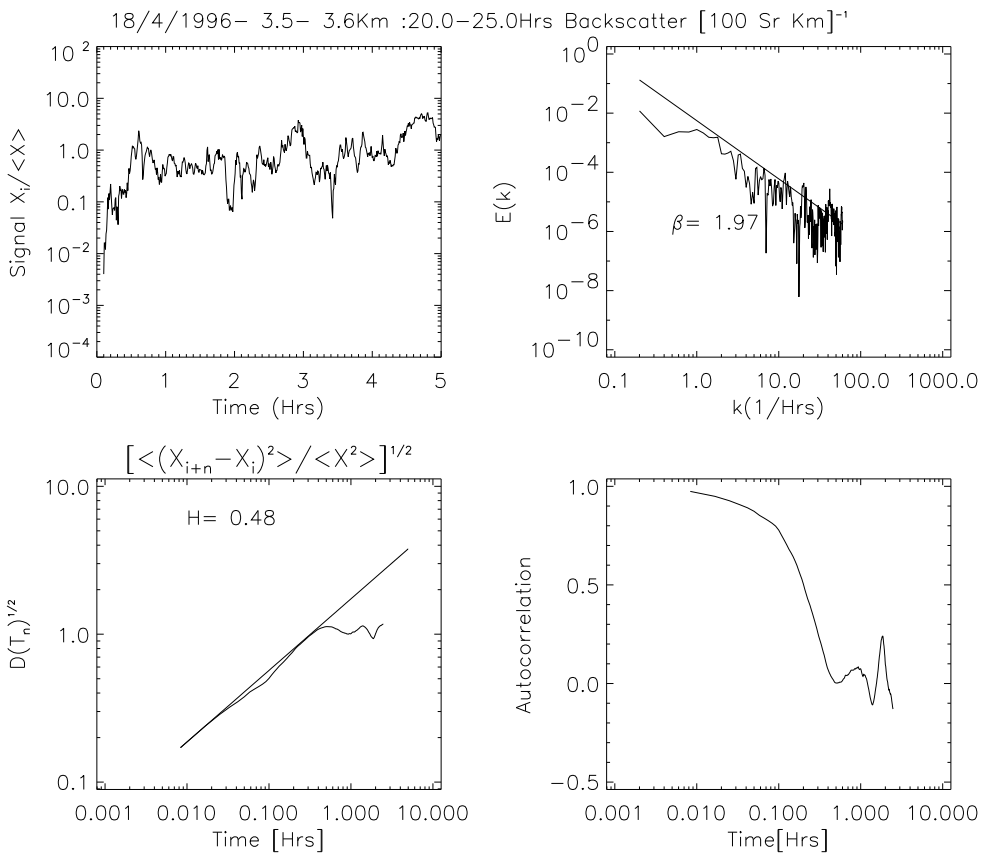

Figure 14: Spectral analysis results for lidar signals of April 18th.

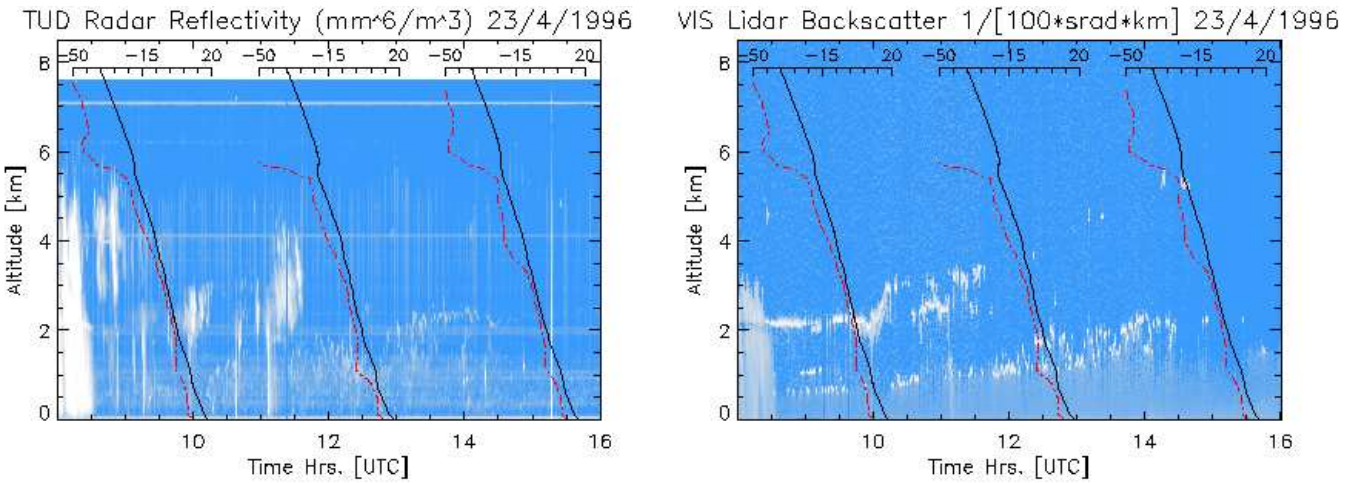

Figure 15: Radar (Left) and lidar (Right) signals for April 23, 1996 (CLARA)

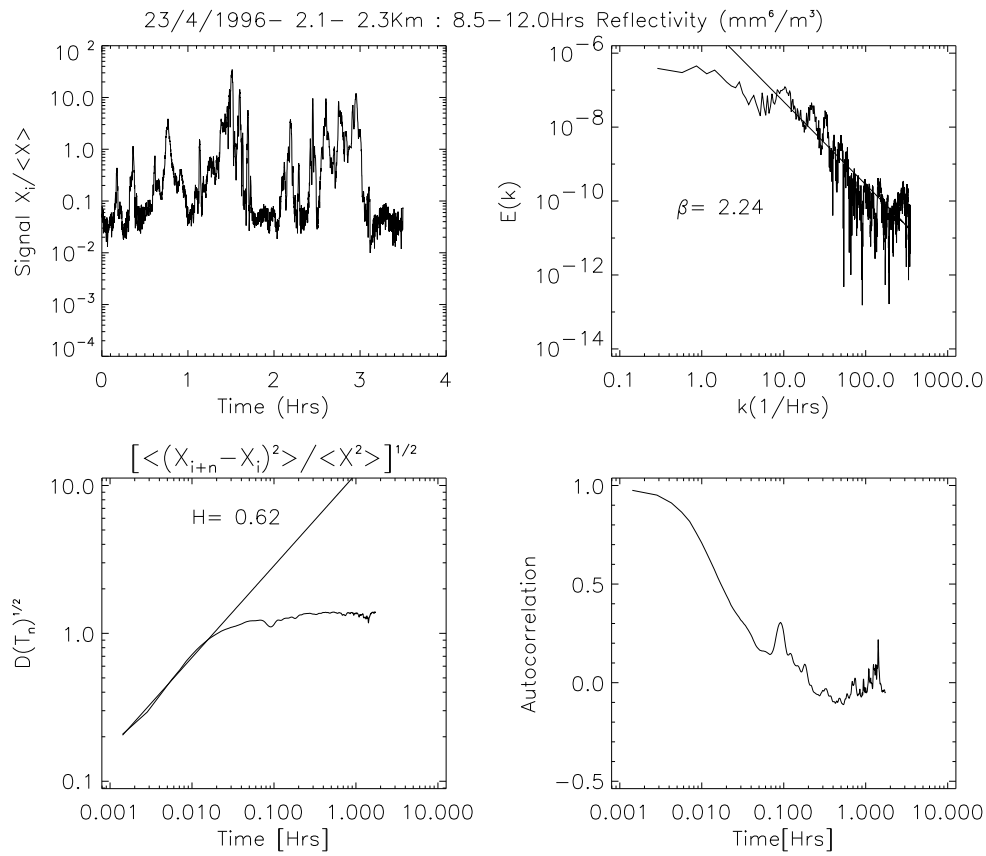

Figure 16: Spectral analysis results for radar signals of April 23, 1996 (CLARA).

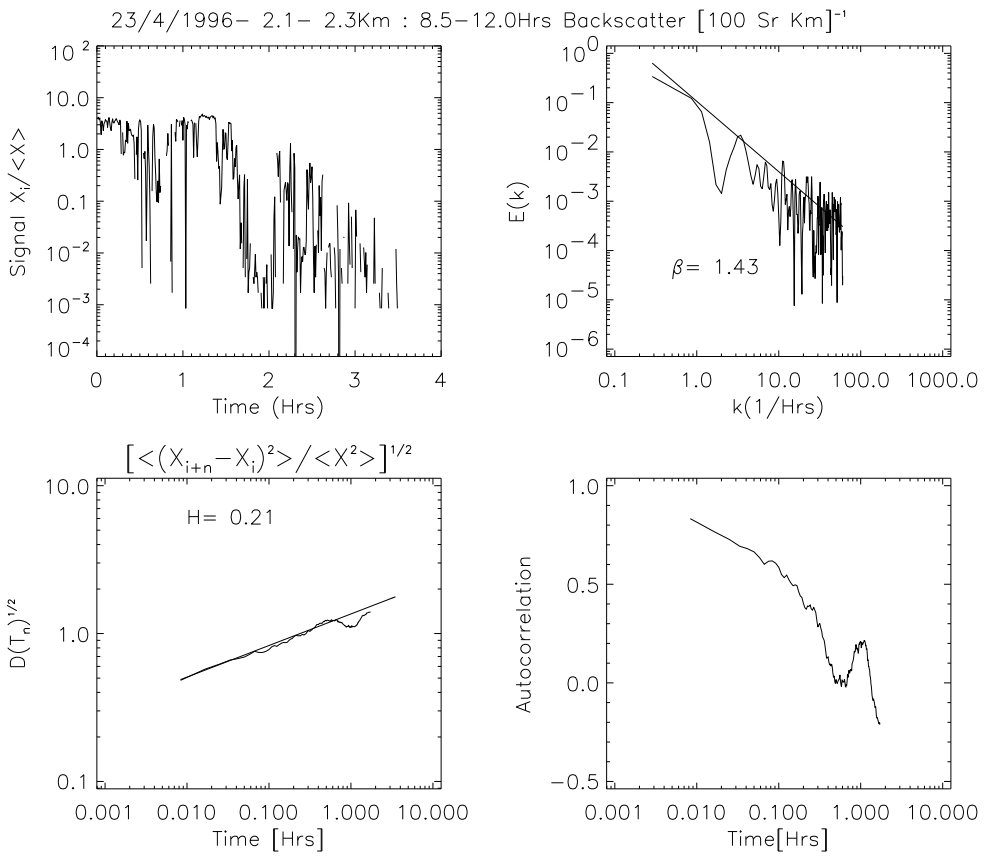

Figure 17: Spectral analysis results for lidar signals in April 23, 1996 (CLARA)

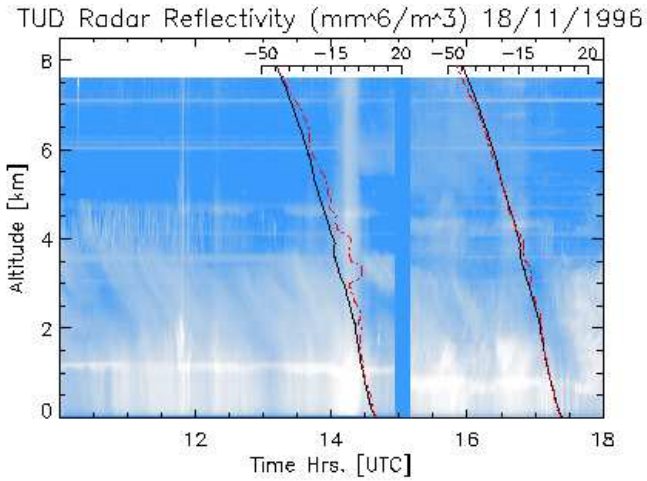

Figure 18: Radar signals for November 18th, 1996 (CLARA).

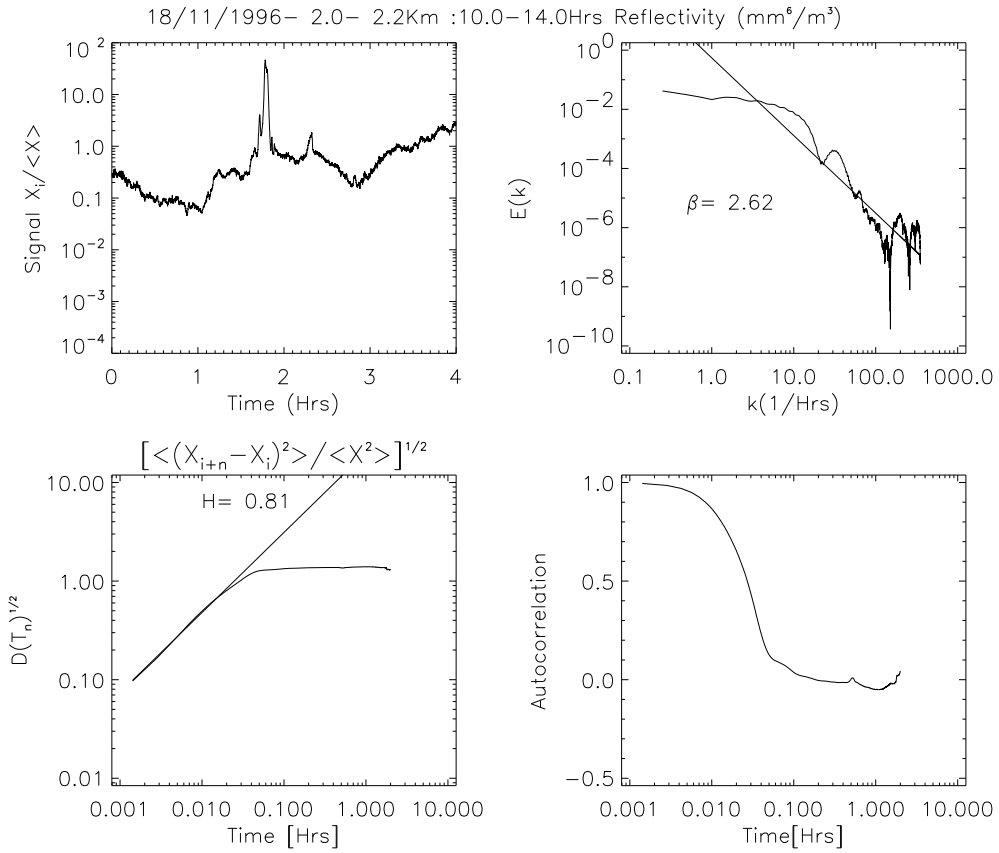

Figure 19: Spectral analysis results for radar signals in November 18th, 1996 (CLARA).

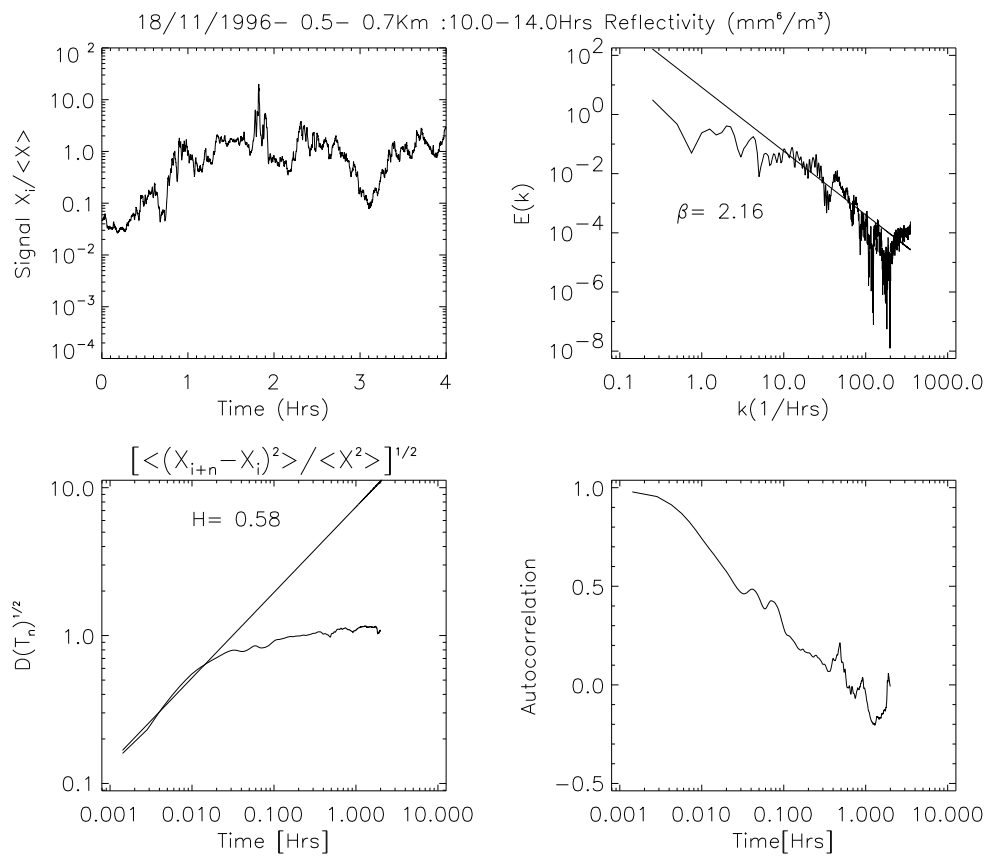

Figure 20: Spectral analysis results for lidar signals in November 18th, 1996 (CLARA)

Summary of Spectral Analysis Results

A summary of the results of the spectral analysis performed on the CLARA data to date is be presented in Table 1.. Here several key parameters have been listed, the point where the PSD (and D) depart from power law behavior, the H exponent, and the time at the correlation coefficient (Acorr) drops to 0.9. It can be seen at a glance that very small correlation times (less than 0.01 Hrs or 0.6 minutes) are much more common than larger ones (over 0.05 Hrs or 3 minutes).

Simulations

Now that we have examined the characteristics of the lidar and radar signals in some detail, we can extend our analysis. We can now proceed to generate 'realistic looking' two dimensional cloud signal fields. The results that will be shown in this section represent an attempt to generalize the inherently 1-d information in the time series data to 2 dimensions and are subject to some limitation, namely a time to space relationship must be assumed (mean-wind-speed) and it must be assumed that the statistical properties of the cloud field are isotropic.

The steps used to generate the signal fields are:

1. First a two dimensional field (of appropriate dimensions) of random numbers is generated.
2. The field is then convoluted with a specified correlation function. The properties of this function (together with a mean-scene wind velocity) determine the PSD and correlation properties of any slice through the resulting field. The resulting numerical field is used to represent the lidar-signal field.
3. A Radar signal field corresponding to the lidar signal field is then generated. This is done using the lidar signal field and specifying a simple model for the relationship between the lidar and radar signals and the underlying particle effective radius and number density.

In practice the random number field was generated using Gaussian random pseudo-random deviates but using uniform deviates changes the initial results little.

To generate the lidar fields correlation functions of the form

$$\left(\frac{1.0}{1.0 + c1 \cdot r}\right)^{cp} \tag{6}$$

where used. In Eqn.(6) r is the radius (distance from the peak of the 2-d correlation function) while $c1$ and cp are adjustable parameters. Generally speaking, $c1$ controls where T_b occurs (the correlation distance) while cp controls the value of H (how fast the correlation decays). An offset and a clipping value were then applied to the field to eliminate negative values. In Fig. 21 an example lidar signal field which mimics conditions roughly similar to those on April 18th, 1996 during CLARA is shown. A cross-section of the signals obtained by taking a horizontal cut through the center of Fig. 21 is shown in Fig. 22.

To generate a reasonable link between the lidar and radar fields a simple mode was used. The lidar signals was considered to be the product of a *number density* (N_o) and an *effective radius* (R'_{eff}) field such that

$$S_{lid} = N_o R'^2_{eff} \tag{7}$$

while the Radar field was given by

$$S_{rad} = N_o R'^6_{eff} \tag{8}$$

For simplicity, the effective radius field (N_o) was linked directly to the lidar signal filed as:

$$R'_{eff} = AS_{lid} + B \tag{9}$$

Where A and B are adjustable parameters. If A is equal to zero then R'_{eff} is constant and the lidar and radar fields will be proportional to each other and will have identical spectral characteristics. For A not equal to zero the lidar and radar fields will have different spectral characteristics. If A is not equal to zero R'_{eff} and N_o will be related as:

$$R'_{eff} = \frac{1 - (1 - 4ABN_o)^{1/2}}{2AN_o} \tag{10}$$

An example scene is shown in Fig. 23 which was generated using the same parameters as those used in the data shown in Fig. 21 except that a coupled lidar and radar field are shown. Fig. 24 shows a lidar and radar signal cross-section taken from the same data used in Fig. 23. Fig. 24 also shows the

Case	Date	Time	Instrument	Alt.(Km)	$T_{break} hours$	H	T(0.9) Hrs
1.	17 Apr	13.5-15.5	Radar	6.0-6.1	0.03	0.4	0.01
			RIVM		0.03	0.37	0.002
2.	18 Apr	20.2-25.0	Radar	3.5-3.6	0.2	0.5	0.02
			Vis		0.4	0.48	0.04
3.	23 Apr	8.5-11.3	Radar	2.1-2.3	0.01	0.6	< 0.001
			Vis		0.5	0.27	< 0.01
4.	26 Apr	7.0-8.4	Vis	7.0-8.4	0.5	0.5	0.02
5.	25 Aug	12.5-19.0	Radar	4.0-4.1	0.02	0.58	0.02
			Vis		0.02	0.37	< 0.01
6.	02 Sep	8.0-16.0	Vis	1.8-2.0	0.04	0.28	< 0.01
7.	18 Nov	10.0-14.0	Radar	0.5-0.7	0.01	0.60	0.004
			Radar	2.0-2.2	0.05	0.79	0.01
8.	19 Nov	0.0-7.0	Radar	0.6-0.7	0.04	0.12	< 0.001
		10.0-12.0	Radar	2.5-2.6	0.02	0.55	0.01
		0.0-8.0	Vis	0.6-0.7	0.02	0.52	< 0.01
		10.0-12.0	Vis	2.5-2.6	0.02	0.51	< 0.01
9.	20 Nov	14.0-22.0	Radar	6.0-6.1	0.07	0.25	0.001
		17.0-22.0	Vis	1.0-1.1	0.03	0.43	< 0.01
10.	29 Nov	1.0-5.0	Radar	5.0-5.1	0.02	0.61	0.01
			Vis		0.05	0.65	0.02
11.	05 Dec	11.0-18.5	Radar	5.0-5.1	0.02	0.2	< 0.001
			Vis		1.0	0.15	< 0.01

Table 1: Summary of current spectral analysis results.

associated time-series analysis. The PSDs, structure functions, and the autocorrelations fall well within the range calculated from the CLARA data set. Here the N_o-vs-R'_{eff} coefficients were chosen so that the lidar and radar fields are similar but not identical to each other.

Once suitable artificial fields which mimic the relevant statistical features of the 1-D CLARA data sets have been created one is then able to fly lidars and raiders with different sampling characterizes (footprint, shot separations, spatial and temporal offsets) over the generated scenes. Effective radius and volume retrievals are then carried out using the lidar and radar signals and the results compared with the true values.

Two examples are shown in Figs. 25 and 26. In Fig. 25 the left panel shows various signal time (distance) series that would have been measured by an instrument overflight with the specified sampling rate and beam footprint for different spatial offsets. The effective radii retrieved using the lidar and various radar signal pairs are also shown. The right panel shows the corresponding fraction of points whose error exceeds 100 %. In this case, even spatial offsets on the order of the radar footprint (here 0.5 km) can be seen to cause significant errors in the effective radius determination. Fig. 26 is similar to Fig. 25 except that the right panel shows the fraction of points in error in excess of 50 %.

Conclusion

Various simulations (though admittedly not exhaustive) have been conducted along the lines of those shown in the last section. It is hard to formulate any general rules. As even for cases in which the broad statistical parameters derived from the spectral analysis appear to be the same the errors turn out to depend in a strongly random fashion on the exact paths chosen for comparison. Very many systematic runs would have to be conducted for a given set of parameters before

any meaningful hard statistics could be generated. However, this in itself is a useful result. This observation implies that the error due to any spatial and/or temporal separation between the lidar and radar orbits would be very hard to quantify in practice. Even if the general 'cloud field type' being observed were known the errors encountered in practice may be 'all over the board' likely making any kind of correction unfeasible.

The investigation of 'cloud variability' is not yet complete, in the sense that we have not produced a definitive hard answer to the question "under general circumstances how much time and spatial difference may be allowed between two observations if we want to meaningfully compare them ?". However, the question we have been trying to answer is somewhat ill-posed and trying to produce an exact answer to such a question may not be feasible. However putting all the evidence gathered in this study together the upper range of the answer is certainly "not much time (under a minute) and not much space (under a km)" with the lower range being still somewhat undefined.

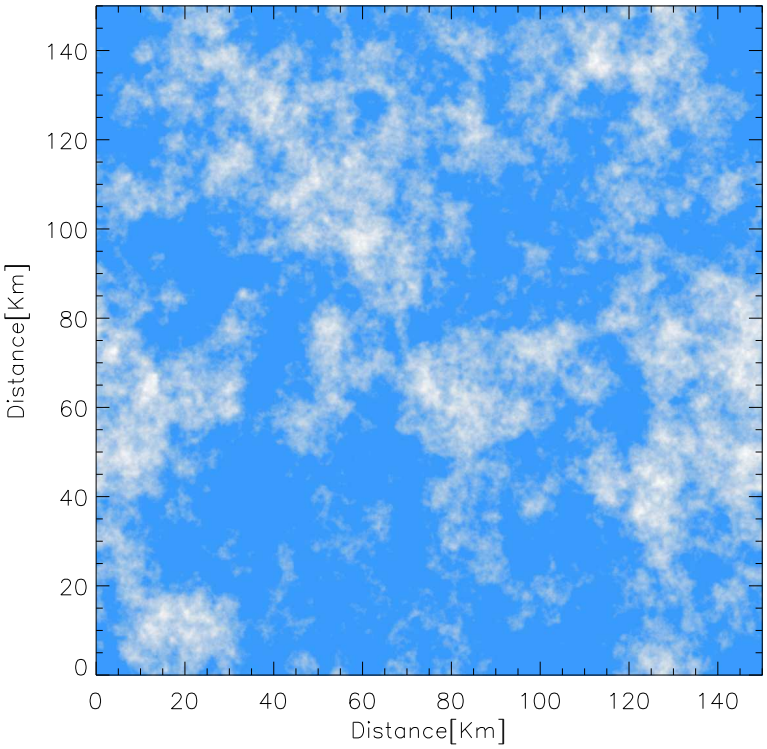

Figure 21: Synthetic 2-dimensional Lidar signals representative of a situation similar to April 18th, 1996 (CLARA)

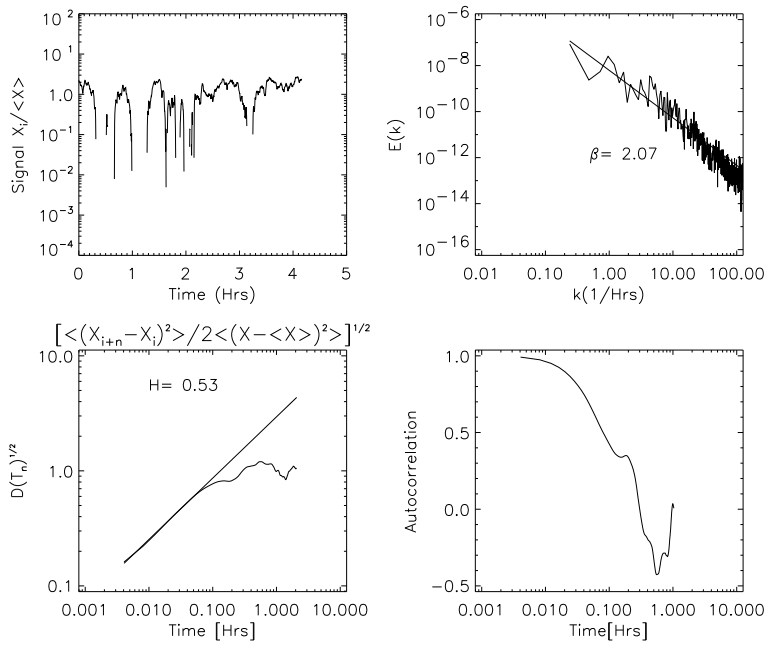

Figure 22: The top left panel shows lidar signals taken from a slice through the data shown in Fig. 22. The other panels show the PSD, structure function, and the autocorrelation coefficient of the signals respectively.

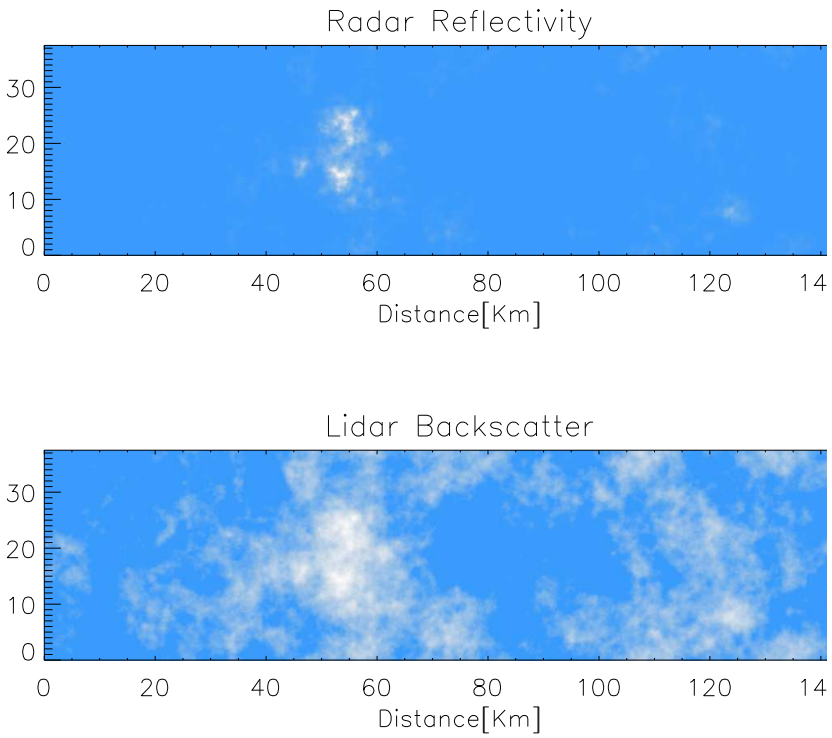

Figure 23: Synthetic 2-dimensional Lidar (Bottom) and Radar (Top) signals representative of a situation similar to April 18th, 1996 (CLARA)

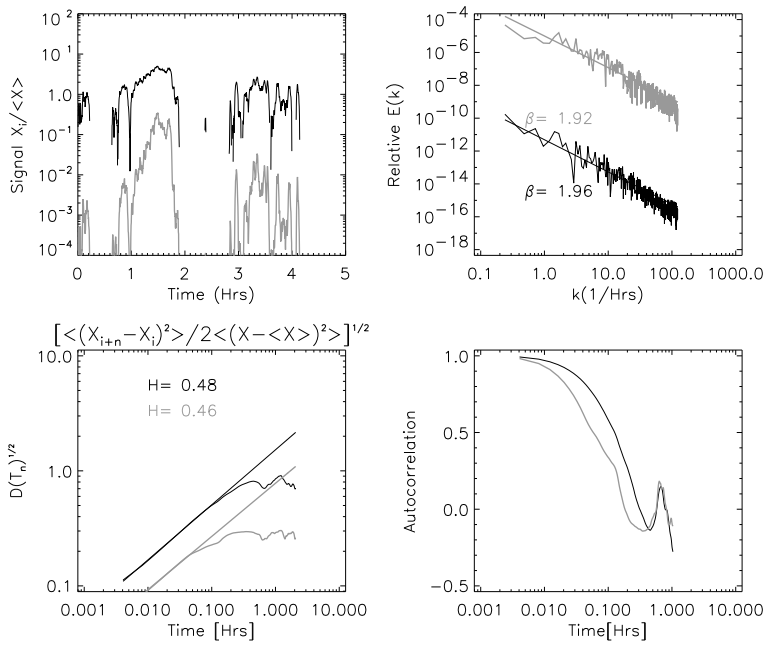

Figure 24: The top left panel shows lidar (dark thin line) and radar (thick Grey line) signals taken from a slice through the data shown in Fig. 23. The other panels show the PSD, structure function, and the autocorrelation coefficient of the signals respectively.

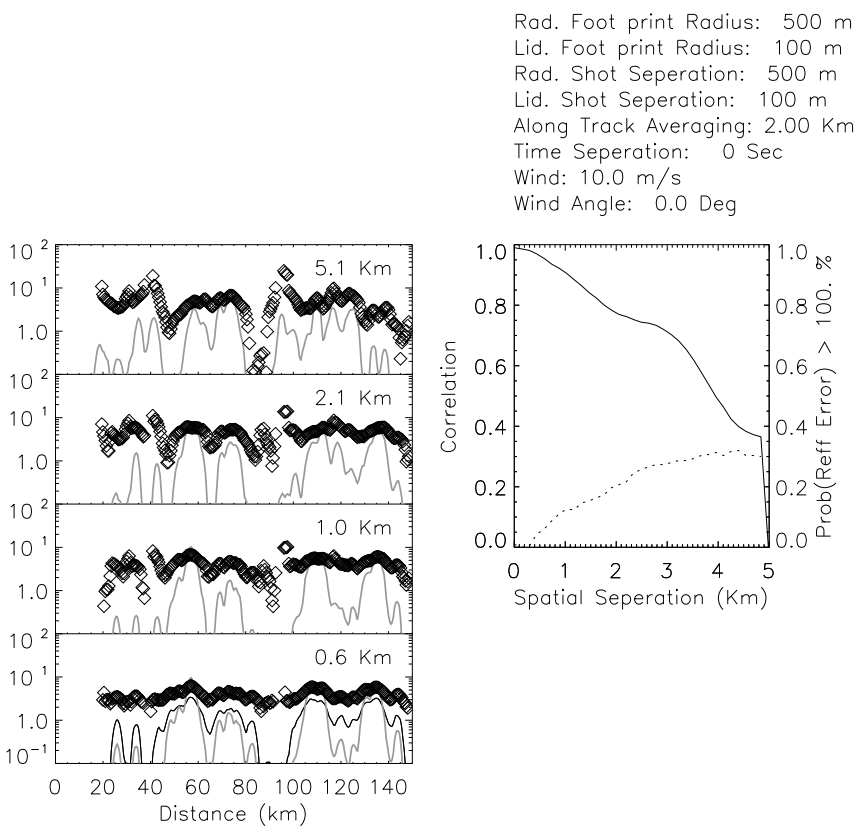

Figure 25: Left Panel: Lidar signals generated from an 'overflight' of the data shown in Fig. 24. Here the thin dark line shows the lidar signal while the Grey lines show radar signals for various tracks that are offset from the original lidar track. The numeric label gives the location of the overpass relative to the bottom of the image The diamonds show the results of various effective radius retrievals using the various lidar and radar signal pairs. The right panel shows the fraction of measurements in error by more than 100 % compared to the true values of the effective radius along the lidar track.

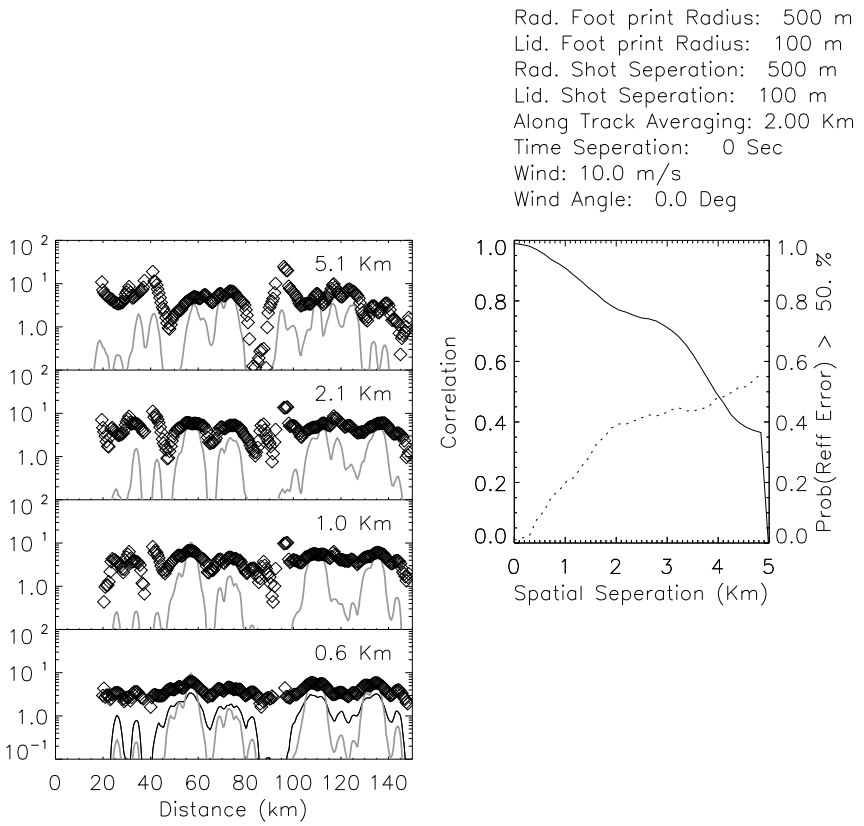

Figure 26: As Fig. 25 except that the threshold in the right panel has been lowered to 50 %

References

Davis A., A. Marshak, W. Wiscombe, and R. Cahalan, Scale Invariance of Liquid Water distributions in Marine Stratocumulus Part 1: Spectral Properties and Stationarity Issues, *J. Atmos. Sci.*, **53**, 1538-1558, 1996.

Donovan, D., A.C.A.P van Lammeren, A. Feijt, H. Bloemink, H. Russchenburg, A. Apituley, Analysis of ERM synergy by use of CLARA observations, Study note 1: Description of Selected Data Sets, KNMI, ESA contract No 12953/98/NL/6D , 1998.

Lammeren, A.C.A.P, Russchenberg ,H., Apituley, A., Brink H.T., and Feijt A., CLARA: a Data Set to Study Sensor Synergy, in *Synergy of Active Instruments in the Earth Radiation Mission, 12-14 November 97, Geesthacht*, Quante W., Baptista, J.P.V., and Raschke E., Eds., ESA EWP-1968 – GKSS 98/E/10, 157-160, 1998.